Glide Symmetry Applied to Printed Common-Mode Rejection Filters

Boules A. Mouris, *Member, IEEE*, Armando Fernández-Prieto, *Senior Member, IEEE*, Jose L. Medrán del Río, *Graduate Student Member, IEEE*, Ragnar Thobaben, *Member, IEEE*, Jesús Martel, *Senior Member, IEEE*, Francisco Mesa, *Fellow, IEEE*, Francisco Medina, *Fellow, IEEE*, and Oscar Quevedo-Teruel, *Senior Member, IEEE*

***Abstract*— In this article, we present a novel application of glide symmetry to differential lines with common-mode (CM) rejection filter properties. Two different topologies are investigated. First, glide symmetry is applied to a pair of differential lines where ground-connected mushrooms are employed as a CM rejection structure. The same idea is also used in a pair of differential lines where defective ground structures are introduced to stop the CM propagation. It is demonstrated that the CM rejection bandwidth is drastically increased when glide symmetry is exploited in both topologies when compared with their corresponding structures without glide symmetry. Furthermore, we show that the differential-mode propagation is hardly affected by the use of glide symmetry, ensuring the good integrity of the transmitted information. Experimental demonstration for both mushroom and defected ground structure is provided. Good agreement between simulations and measurements results is observed.**

***Index Terms*— Common-mode (CM) rejection filters, differential lines, glide symmetry.**

I. Introduction

THE interest in the study of balanced differential architectures that operate at microwave frequencies has experienced significant growth during the last 15 years, especially in what concerns the implementation of filters and other passive devices. Differential signaling is also essential in high-speed digital transmission. In general, differential circuits tend to be more complex and to occupy a larger substrate area than their single-ended counterparts. However, differential balanced structures are a very attractive choice for present and future wireless devices because of their multiple advantages associated with higher robustness to environmental noise, lower electromagnetic interference problems, and lower power consumption. The reader can find extensive literature reviews on microwave balanced passive devices in several books and review articles, for instance, [1]–[4].

Multiple examples of passive devices implemented with printed circuit technology can be found in more recent literature; for instance, single-to-balanced power dividers [5], balanced rat-race couplers [6], coupled-line couplers [7], balanced wideband phase shifters [8], and dual-band balanced filters [9]. Most of these devices are designed to strongly suppress the common-mode (CM) signal while preserving the desired differential-mode (DM) response within the frequency band(s) of interest. This is usually carried out through the reflection of the CM signal. Nevertheless, recently, balanced devices with an absorption mechanism to suppress the CM contribution have been proposed [10]–[13]. In any case, the above designs are mostly based on the use of symmetrical structures that incorporate either printed distributed or lumped soldered components to provide, simultaneously, the required DM response and the suppression of the undesired CM signal. This methodology requires searching for smart topologies and layouts that lead to the fulfillment of this double goal. However, an obvious alternative solution is to combine any DM design (without taking care of the CM response) with a properly chosen CM rejection filter, which can be connected to one or more ports of the balanced device. This procedure is sometimes unavoidable to add CM rejection to some specific designs, as reported for example in [7]. This article follows this strategy and will show two advantageous designs of CM filters operating at microwave frequencies and fabricated in planar technology.

A widespread manner of implementing CM rejection filters at microwave frequencies is based on the use of a pair of periodically loaded balanced transmission lines. These structures are symmetric with respect to a longitudinal plane, in such a way that no CM to DM conversion is theoretically possible (namely, the structure supports two fundamental modes: even and odd). Besides, the periodic loadings should not affect the DM component of the whole electromagnetic field whereas it strongly interacts with the CM contribution. The final result is that the structure is transparent for the DM signal, and

Manuscript received May 5, 2021; revised September 5, 2021; accepted October 11, 2021. Date of publication December 1, 2021; date of current version February 7, 2022. The work of Armando Fernández-Prieto, Jesús Martel, Francisco Mesa, and Francisco Medina was supported in part by the Spanish Agencia Estatal de Investigacion, Ministerio de Ciencia e Innovacion, under Grant MCIN/AEI/10.13039/501100011033/; in part by the "ERDF A way of making Europe" under Project EC2017-84724-P. *(Corresponding author: Boules A. Mouris.)*

Boules A. Mouris, Ragnar Thobaben, and Oscar Quevedo-Teruel are with the School of Electrical Engineering and Computer Science, KTH Royal Institute of Technology, 10044 Stockholm, Sweden (e-mail: boules@ieee.org).

Armando Fernández-Prieto, Jose L. Medrán del Río, and Francisco Medina are with the Departamento de Electrónica y Electromagnetismo, Facultad de Física, Universidad de Sevilla, 41012 Seville, Spain.

Jesús Martel is with the Departamento de Física Aplicada 2, ETS de Arquitectura, Universidad de Sevilla, 41012 Seville, Spain.

Francisco Mesa is with the Departamento de Física Aplicada 1, ETS de Ingeniería Informática, Universidad de Sevilla, 41012 Seville, Spain.

Color versions of one or more figures in this article are available at https://doi.org/10.1109/TMTT.2021.3127933.

Digital Object Identifier 10.1109/TMTT.2021.3127933

at the same time, a stopband filter is implemented for the CM one. The forbidden band for the CM can be caused either by Bragg reflections, which lead to electrically large structures or by the resonances of loading components, which could be electrically small. Several examples illustrating this approach are discussed in [1] and references therein. On the other hand, periodic structures of this type (i.e., electromagnetic bandgap—EBG—filters and other similar configurations) have also been used extensively to implement single-ended stopband filters (see, for instance, [14], [15] and references therein). However, it has not been until very recently that the advantages of introducing glide symmetry in the unit cell of such kind of devices has been explored. In [16], a single microstrip line is coupled to a periodic distribution of identical resonators consisting of printed patches having a ground via at one of their ends. This could be seen as a microstrip line coupled to a 1-D mushroom structure, something very similar to the structure proposed in [11]. But the key idea in [16] is that if the unit cell of the mushroom structure incorporates glide symmetry by alternating the positions of the ground vias in adjacent patches, a significant increase of the bandwidth of the rejected band is achieved when compared with the conventional (non-glide) implementation. This result is relevant from a theoretical point of view and as a proof of concept, but the performance of the device as a bandstop filter is not optimum due to the poor matching out of the rejected band. However, this drawback should not be a problem when the purpose of the device is to provide CM rejection in a differential periodic transmission line where there are no specific requirements for the CM response outside the frequency band to be suppressed.

Different from our previous work in [16], which focused on improving the bandwidth of operation of single-ended excitation of mushroom-type EBG structures using glide-symmetric edge-located vias, here we propose and study a novel application of glide symmetry to periodically-loaded differential lines. First, we investigate periodic loading with glide-symmetric mushrooms similar to those in [16], and then we propose a glide-symmetric DGS design as a convenient fully planar alternative. We show that, compared to the conventional (non-glide) periodic implementation, the glide-symmetric versions exhibit a significantly wider and deeper stopband for the CM response while keeping an all-pass behavior for the DM, as desired. Moreover, we present the equivalent circuit model for CM operation in the structures under study. It is found that the only drawback of glide-symmetric structures is some small level of mode conversion, which is absent in non-glide structures having a longitudinal symmetry plane. Thus, as long as this low level of mode conversion is tolerable, the advantages associated with the glide-symmetric structures justify the choice of this solution.

This article is organized as follows. Section II describes the differential version of the structure reported in [16]. It is shown how this pair of balanced transmission lines, coupled to a periodic 1-D mushroom-like structure, benefits from the introduction of glide symmetry in comparison with a non-glide implementation. In particular, a larger bandwidth and increased CM rejection level are achieved by simply alternating the positions of the grounding vias. A similar strategy is applied in Section III to an alternative structure that does not require grounding vias. This structure can be considered the glide-symmetric version of the non-glide configuration reported in [17], and it is based on the coupling of the pair of balanced microstrips to a properly designed defected ground structure (DGS). Once again, the superiority of the configuration that incorporates glide-symmetric cells is demonstrated. Appropriate circuit models are presented and validated in Sections II and III for both structures through simulations and measurements. Finally some concluding remarks are summarized in Section IV.

II. Differential Lines Loaded With Grounded Mushrooms

Mushroom structures with central vias have long been studied for EBG operation [18] as well as microstrip filter applications [14], [15], [19], [20]. Apart from the interesting properties of mushroom structures with central vias, they tend to have a relatively large electrical size. Mushroom-type EBG structure with edge-located via has been presented in [21] as a solution for size reduction. However, this solution came at the cost of losing some bandwidth performance when compared to central vias design. In our previous work [16], we investigated the application of higher symmetries, specifically glide symmetry, to mushroom-type EBG structures with edge-located vias. It was demonstrated that introducing glide symmetry can significantly enhance the operation bandwidth with no additional manufacturing cost. The bandwidth enhancement was attributed to the stronger field confinement inside the glide structure, which gives rise to a stronger coupling between sub-unit cells and, thus, improved bandwidth. This feature was verified through demonstrations of the fields inside the structure, simulation, and experimental results, as well as providing an accurate circuit model.

In this work, we investigate the effect of applying glide-symmetry to mushroom-type EBG structures in a differential line setup for CM suppression. In structures excited using differential lines, it is generally desired an all-pass response for the differential mode (DM) as well as a good rejection bandwidth for the CM noise. Here, we design and study the response of a CM rejection filter consisting of differential lines loaded with grounded mushrooms with/without glide symmetry. The structures under study are illustrated in Fig. 1. Each structure consists of a pair of microstrip lines on the top substrate loaded, in the middle substrate, with square-shaped mushrooms that are grounded using edge-located vias. The unit cells of each of the studied structures are highlighted with black dashed lines in Fig. 1(a) and (c) and shown separately in (b) and (d), respectively. As explained in [16], a unit cell of the glide-symmetric structure along the propagation (x) direction is obtained by translating the sub-unit cell (which contains only one grounded mushroom) by half the period length along the x-axis and then mirroring it with respect to the y-plane. It should be noticed that twice the physical period length in the x-direction is chosen for the

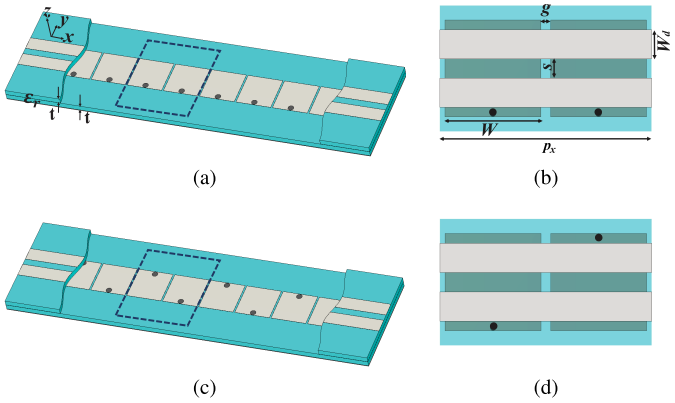

Fig. 1. Differential lines loaded with grounded mushrooms. (a) Conventional structure and (b) its unit cell. (c) Glide-symmetric structure and (d) its unit cell. The period of the unit cell shown in (b) is taken as twice its actual physical period for convenient comparison with the unit cell in (d).

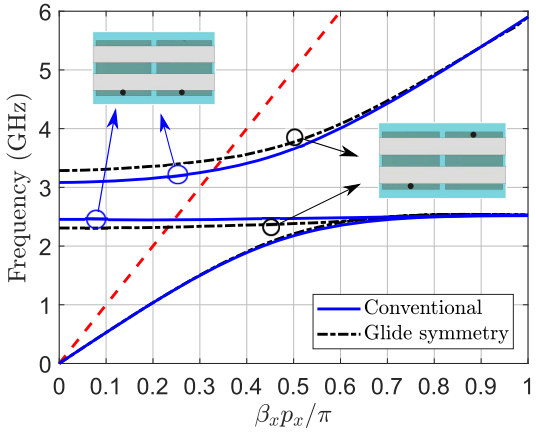

Fig. 2. Dispersion diagram for CM operation for the conventional and glide-symmetric structures illustrated in Fig. 1. Data obtained using *CST Microwave Studio* eigenmode solver.

conventional structure to have a more appropriate comparison with its corresponding glide-symmetric version.

Following a similar design procedure as in [16, Sec. V-B], a dielectric substrate of $\epsilon_r = 3.48$ and thickness $t = 1.524$ mm is chosen (commercial Rogers 4350B substrate). The dimensions of the structures are designed to have bandgap operation at frequency $f_0 \approx 3$ GHz. In general, for mushroom-type EBG structures with edge-located vias, the high impedance condition is achieved when the width of the metallic patch is approximately $\lambda_{\epsilon_r}/4$. However, when the separation between the patches is small (i.e., strong coupling exists between adjacent patches), the patch size is effectively smaller [16], [21]. In our design, the gap size between the mushroom elements is selected to be $g = 0.5$ mm in order to provide a wide rejection bandwidth. In principle, a smaller gap size would provide a wider bandwidth due to stronger coupling between the sub-unit cells [16, Sec. V]. However, we selected the gap size to be $g = 0.5$ mm in order to facilitate the manufacturing process. The corresponding width of each square mushroom element is $W = 7$ mm. The above design makes a periodicity along the propagation direction of $p_x = 15$ mm. Similar to [16], the radius of the vias is $r = 0.1$ mm. It should be noted that varying the via radius changes the effective width of each mushroom element as well as its inductance to the ground, which finally causes a change in the resonance frequency. In order to achieve good matching for the DM, the width of each microstrip line on the top layer is taken as $W_d = 6.7$ mm with separation distance $s = 4$ mm.

A. Unit-Cell Study and Dispersion Diagram

In order to study the CM rejection bandwidth of the proposed structures, the unit cells in Fig. 1(b) and (d) are simulated in CM operation by means of the eigenmode solver of *CST Microwave Studio*. The obtained dispersion diagrams of the first passing and stopping bands are plotted in Fig. 2. As reported in [16], compared to the conventional unit cell, applying glide symmetry results in increasing the impedance associated with the fundamental mode as well as increasing the cutoff of the first higher-order propagative mode. Exploiting these two features, the bandgap observed in Fig. 2 for the glide-symmetric unit cell is significantly wider than the conventional one. Consequently, a wider CM rejection bandwidth is thus expected by using glide symmetry.

B. Equivalent Circuit Model

Following a similar rationale as in [16], an equivalent circuit model for the CM operation of the unit cells in Fig. 1(b) and (d) is shown in the insets of Fig. 3. In fact, the topology of this equivalent circuit is similar to the one proposed for the mushroom-type EBGs with edge-located vias described in [16, Sec. IV]. The only slight difference comes from the procedure to calculate the circuit parameters related to the top microstrip lines. In principle, the lack of symmetry with respect to the middle vertical plane ($y = 0$) between the coupled microstrip lines makes that the CM analysis of the structure cannot be strictly reduced to a single line with a magnetic wall in that middle plane, as described in [2, Ch. 2] for symmetrical lines. Here, we assume that the pair of microstrip lines can be modeled using the values of L_U and C_U (inductance and capacitance as defined in [16]) computed for these coupled lines considering that the structure is symmetric. A validation of this assumption is given in the Appendix. In addition, due to the relatively large width of the top microstrip lines in our design, their capacitance to the ground plane cannot be neglected and is modeled by C_B. As shown in the circuit model inserted in Fig. 3(a), the isolated grounded mushroom is modeled with a patch inductance, L_p, a patch capacitance, C_p, and the via inductance, L_v. Thus, the obtained equivalent circuit should generate the correct CM response, considering 25-Ω (25-Ω being the value of the characteristic impedance of the common mode).

For the computation of the inductances L_p and L_U, we follow [16] and make use of the formula provided in [22] as

$$L = \frac{Z\sqrt{\epsilon_{\text{eff}}}}{c} l \tag{1}$$

where Z and ϵ_{eff} are the corresponding impedance and effective dielectric constant, c the speed of light, and l the length of

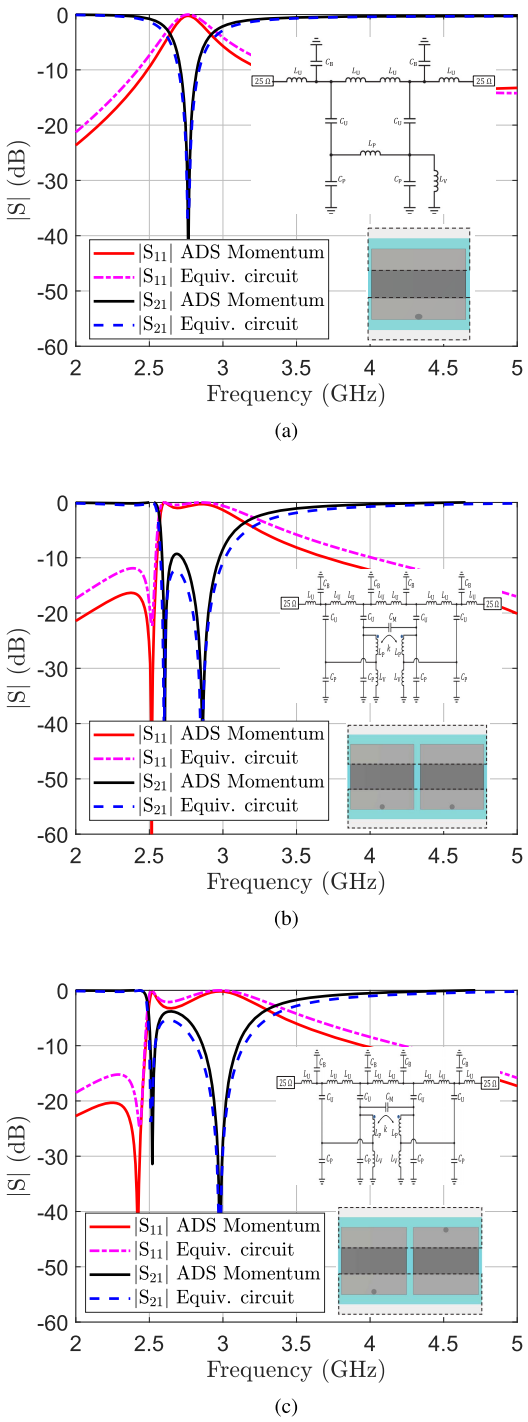

Fig. 3. Comparison of equivalent circuit vs. full-wave simulations for the CM operation of (a) one sub-unit cell, (b) unit cell of the conventional mushroom structure, and (c) unit cell of the glide-symmetric mushroom structure. Insets: each structure and its corresponding equivalent circuit.

the patch/line (W and $p_x/8$, respectively). More specifically, Z is taken as the CM impedance, Z_{CM}, when computing L_U. This impedance is calculated making use of [23] and verified using [24], [25] with the dimensions and substrate described in Fig. 1(b) (i.e., $W_d = 6.7$ mm, $s = 4$ mm, substrate thickness of $2 \times t = 3.048$ mm, and $\epsilon_r = 3.48$). The obtained value for Z_{CM} is 28 Ω and the CM effective permittivity is found to be $\epsilon_{\mathrm{eff}}^{\mathrm{CM}} = 2.73$ by using the formulas in [26]. In the above computation of L_U, we considered that the effect of the mushrooms in the middle layer is negligible since the magnetic-field lines associated with the CM are not expected to be much affected by the presence of these patches (the longitudinal returning CM current will take place via the bottom ground plane rather than via these patches). For the calculation of L_p, the values of Z and ϵ_{eff} are computed using the conventional microstrip line formulas in [26] for free space and taking $W = 7$ mm as the width of the microstrip line and $t = 1.524$ mm as the height of the air substrate.

Likewise [16, Eq. (4)], the inductance of the via is calculated from [27, eq. (3)] using

$$L_v = \frac{\mu_0 t}{2\pi}\left[\ln\left(\frac{t}{r}+\sqrt{1+\frac{t^2}{r^2}}\right)+\frac{3}{2}\left(\frac{r}{t}-\sqrt{1+\frac{r^2}{t^2}}\right)\right] \quad (2)$$

with r and t being the radius of the via and the substrate thickness.

The capacitances C_U and C_B are calculated using the following parallel plate capacitance formula:

$$C = \frac{\epsilon_0 \epsilon_r A_{\mathrm{eff}}}{d} + C_f \quad (3)$$

where A_{eff} is the overlapping area between the two conductors, d is the separation distance, and C_f is the capacitance due to the edge effects. In the calculation of C_U, we consider that this capacitance consists of two identical parallel capacitances. Each of these capacitances is originated by a single microstrip line and the metallic patch in the middle layer. Although in Fig. 1(b) and (d) it might seem that the overlapping area is $W_d \times W$, the separation $s = 4$ mm of the case under consideration makes the present overlapping area be smaller and given roughly by $A_{\mathrm{eff}} = 1.5 \times 7$ mm^2. Here, the value of d is equal to the substrate thickness t. The overlapping area for calculating the capacitance C_B between the top microstrip line and the ground is $A_{\mathrm{eff}} = 5.2 \times 7$ mm^2 with d equals to twice the substrate thickness $2t$. In both cases above, the value of C_f is calculated using the formulation provided in [24] and [25]. The capacitance C_p between the mushroom patch and ground is calculated in a similar way, using the stripline capacitance provided in [24] and [25].

C. Simulation and Experimental Results for the Proposed Differential Lines With Grounded Mushrooms

The numerical values of the circuit parameters obtained from the closed-form approximate expressions given in the above section are provided in the first row of Table I. Some of these parameters have to be tuned to better fit the full-wave behavior of the isolated section (sub-unit cell) shown in the inset of Fig. 3(a). As it can be observed from the second row of Table I, the only parameter that has actually required this further tuning is L_v. This is mainly due to the small separation between the mushroom elements which alters the current on the vias. The very good agreement in $|S_{11}^{\mathrm{cc}}|$ and $|S_{21}^{\mathrm{cc}}|$ observed in Fig. 3(a) between the full-wave results produced by *ADS Momemtum* and those obtained from the equivalent circuit clearly shows the suitability of the proposed circuit approach.

TABLE I
VALUES OF CIRCUIT ELEMENTS (L IN nH AND C IN pF)

	L_U	L_p	L_v	C_U	C_B	C_p
Closed form	0.3	1.22	0.613	0.45	0.55	0.25
Tuned	0.3	1.22	2.08	0.45	0.55	0.25

Although not plotted here, the equivalent circuit also provides an excellent agreement with the full-wave simulation in terms of the phase response of both $|S_{11}^{cc}|$ and $|S_{21}^{cc}|$.

The equivalent circuit of the isolated section is further employed to simulate the behavior of two coupled sections when the vias are located either on the same side or in a glide configuration (namely, the considered unit cells of the periodic structures under study). As shown in the inset of Fig. 3(b) and (c), the coupling between the two sub-unit cells is modeled by means of an inter-patch capacitance, C_M, and a magnetic coupling factor, k, between the two patches of inductance L_p. Different from the mushroom structure described in [16], the electric coupling cannot be neglected here due to the small spacing between the adjacent mushroom elements. The coupling parameters are obtained following the procedure described in [16], [26], and [28]. For the conventional unit cell, they are found to be $C_M = 0.062$ pF and $k = 0.02$ and, for the glide case, $C_M = 0.093$ pF and $k = -0.22$. With these values, we find a very good agreement in Fig. 3(b) and (c) between the equivalent-circuit and the full-wave results. The circuit approach reveals that the electric and magnetic couplings between the sub-unit cells are stronger in the case of glide symmetry. Moreover, the magnetic coupling coefficient has a negative sign in the glide-symmetric case due to the change in the orientation of the patch currents. The above observations have been discussed in detail in [16], [29] and are be attributed to the properties of glide-symmetric structures.

As a final step to study the DM and the CM operation of the proposed structures, two finite structures consisting of five unit cells in the x-direction (i.e., ten mushroom elements) were simulated, fabricated, and measured. A picture of one of the fabricated prototypes is shown in Fig. 4(a). The simulated S-parameters obtained from *CST Microwave Studio* are compared to the measured S-parameters for the conventional and the glide-symmetric structure in Fig. 4(b) and (c), respectively. It can be observed from the simulated and measured results that, for the DM operation, an all-pass response is obtained for both the conventional and the glide-symmetric structures with a very good matching level ($S_{11}^{dd} < -15$ dB). The measured (simulated) CM rejection bandwidth calculated at -20 dB rejection level is 0.52 (0.65) GHz for the conventional structure and 0.81 (0.97) GHz for the glide structure. The discrepancies between the measured and simulated results are attributed to the inaccuracies in the multi-layer manufacturing process; namely, the increased permittivity and thickness as well as the possible presence of air gaps due to the use of RO4450F bondply to adhere the layers together. Nevertheless, both simulated and measured results indicate a significantly wider CM rejection bandwidth in the glide-symmetric case.

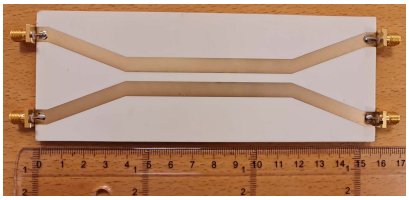

(a)

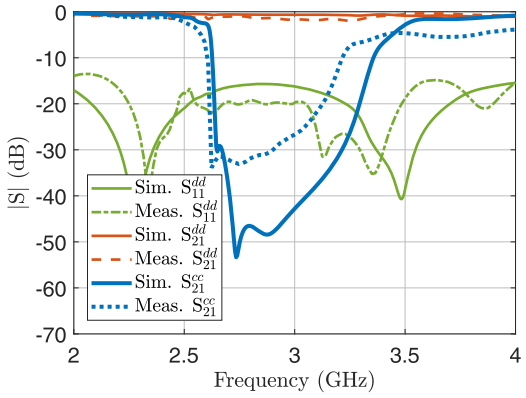

(b)

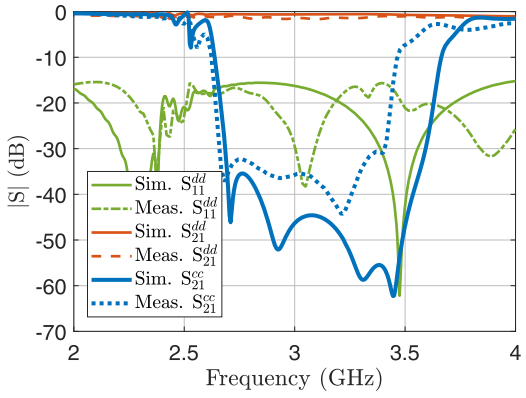

(c)

Fig. 4. (a) Photograph of one of the fabricated structures. (b) and (c) Simulated and measured DM and CM responses for the structures described in Fig. 1 with 10×1 square-shaped mushrooms. (b) Conventional structure. (c) Glide-symmetric structure.

This very substantial increase of the operational band clearly confirms the ability of glide symmetry to widen the CM rejection bandwidth without affecting the DM operation and with no extra manufacturing costs.

In Fig. 5, the measured differential eye diagrams for the conventional mushroom structure and that of the glide symmetric version are shown. An excitation of amplitude 0.2 V in 2.5 Gb/s was used for the measurements. The conventional structure shows a 330.47 mV eye height, a 390-ps eye width, and an opening factor of 0.88. For the glide-symmetric structure, the eye height is 321.5 mV, the eye width is 392 ps, and the opening factor is 0.86. It can be concluded that, although the glide-symmetric structure provides a wider CM rejection bandwidth, it provides almost the same signal integrity performance for the DM as the conventional structure.

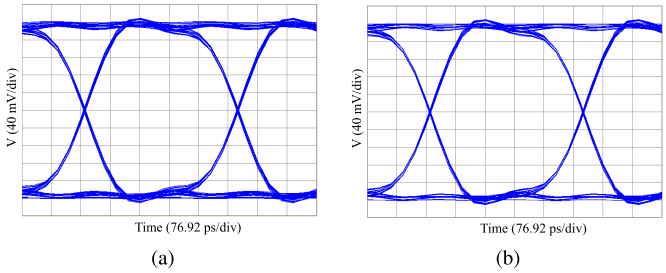

Fig. 5. Measured eye diagrams for the DM of (a) conventional mushroom structure and (b) glide-symmetric mushroom structure.

III. Differential Lines Loaded With Defected Ground Structure

Defected ground structures (DGS) are very popular in microwave planar technology. In fact, DGSs have been applied to almost any planar device, as reported in the specialized literature [2], [30]–[32]. In the context of differential signals, DGSs are excellent candidates for the design of differential lines when strong CM rejection is required, mainly thanks to their good electromagnetic performance and their ease of design and integration into planar technology. Usually, DGSs are symmetrically located below the coupled differential pair in order to ensure both good DM transmission and a high level of CM noise rejection. However, in this section, it will be shown that such total symmetry is not fully imperative for good DM operation. In the same way, as differential lines loaded with grounded mushrooms, the use of glide symmetry can also improve the CM performance of DGS-loaded differential lines without affecting DM transmission. Specifically, our results will show that, when compared with conventional symmetry, glide symmetry provides higher CM rejection bandwidth as well as a stronger CM rejection level.

A. Proposed Defected Ground Structures and Their Equivalent Circuit Model

The proposed differential lines to be studied are shown in Fig. 6(a), (c), and (e), where DGSs with different symmetries have been included below the coupled microstrip lines. More detailed top views of the unit cells of these periodic structures are depicted in Fig. 6(b), (d) and (f). The configuration in Fig. 6(b) is the most common way of implementing DGSs in differential lines given its symmetry with respect to the longitudinal plane AA' [17]. Although such symmetry is considered critical to ensure both good DM operation and strong CM noise rejection without increasing mode-to-mode conversion, our results will show that this symmetry is not indispensable. To this aim, the modified structures depicted in Fig. 6(c) and (e) are considered. The modal conversion observed in the structure of Fig. 6(e) is briefly discussed in the Appendix, showing that the undesired mixing-mode behavior is kept sufficiently low.

Our analysis starts with the structure in Fig. 6(a), which is a slightly modified version of the configuration proposed in [17] (in that work, the straight strips of length l_{sd} were meanders lines and the ground plane was more slotted). Under

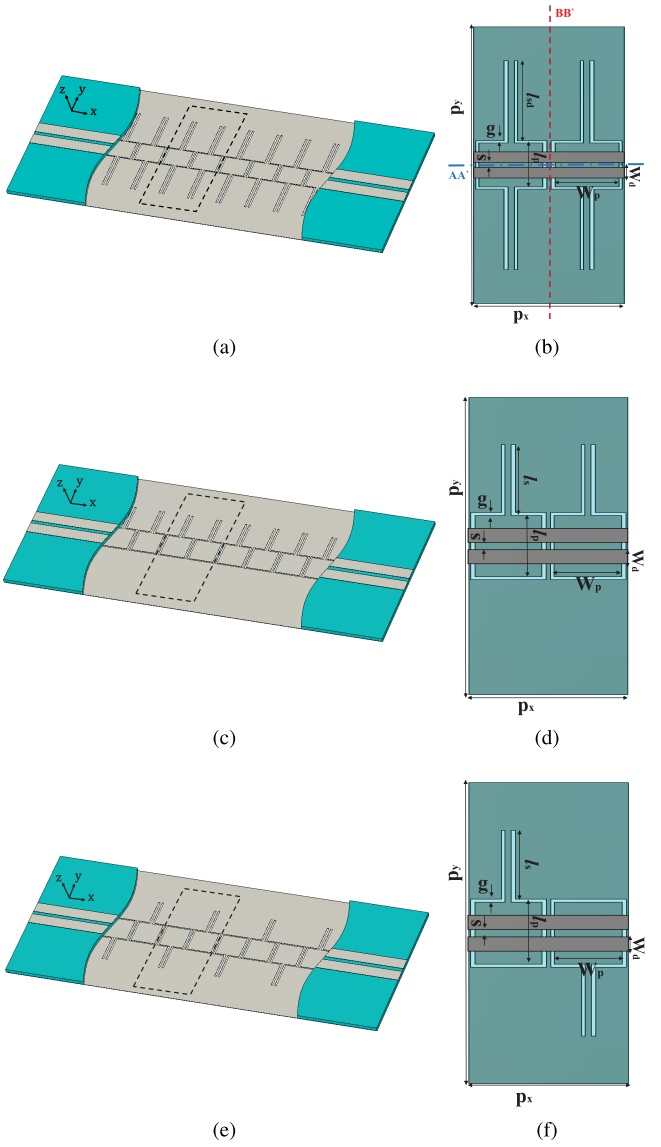

Fig. 6. Differential lines loaded with defected ground structure and their corresponding unit cells. (a) Symmetrical structure with respect to plane AA' and (b) its unit cell. (c) Nonsymmetrical structure and (d) its unit cell. (e) Structure with glide symmetry and (f) its unit cell. The period of the unit cell shown in (b) and (d) is taken as twice its actual physical period for convenient comparison with the unit cell in (f).

DM operation, the symmetry plane AA' of the structure in Fig. 6(a) behaves like a virtual electric wall and, then, the DGS is short-circuited at both ends. It means that, in DM operation, the defected pattern in the ground has almost no influence on the signal propagation since it closely behaves like a conventional ground plane. The pair of coupled lines is thus working as an all-pass filter for the DM operation [17]. On the contrary, under CM operation, the symmetry plane AA' behaves like a virtual open circuit. Since the defected pattern is no longer short-circuited at both sides, its behavior is quite different from a solid ground plane and CM propagation is expected to be affected by the presence of the DGS [2], [17]. A similar structure to that in Fig. 6(a) was reported in [17] to act like an elliptic low-pass filter for the CM

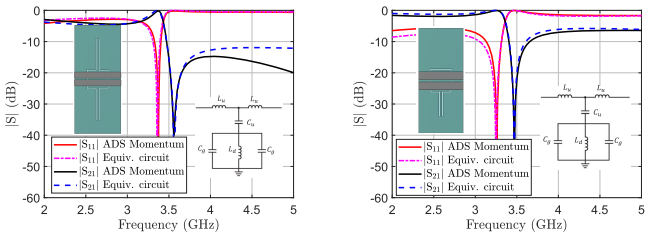

Fig. 7. Comparison of equivalent circuit versus full-wave simulations for the CM operation of (a) symmetric DGS sub-unit cell and (b) asymmetric DGS sub-unit cell. Insets: each structure and its corresponding equivalent circuit.

operation. Following the design procedures described in [17], the structure in Fig. 6(a) has been synthesized to have a transmission zero at a frequency $f_0 = 3.3$ GHz with the following dimensions (in mm): $l_{\text{sd}} = 9.8$, $l_p = 4.3$, $W_p = 3.3$, $g = 0.2$, $s = 0.3$, and $W_d = 1$. A Rogers RT/duroid 5880 substrate ($\epsilon_r = 2.2$) with thickness 0.508 mm is selected for the design.

The symmetry of the structure in Fig. 6(a) makes that the analysis of the coupled microstrip pair can be carried out by considering a single microstrip subject to the appropriate electric/magnetic wall in the symmetry AA' plane. Thus, its corresponding lumped-element equivalent circuit will provide a convenient insight into the wave propagation in this structure. A sub-unit cell of the structure as well as its corresponding equivalent circuit are shown in the insets of Fig. 7(a). In the proposed equivalent circuit model, L_u represents the inductance of one of the top microstrip lines and C_u the capacitance between the top microstrip line and the capacitive patch of length l_p and width W_p. The gap capacitance between the patch and the ground plane is denoted as C_g. L_d represents the inductance of the patch (L_p) added in series with the inductance of the narrow strip (L_s) of length l_{sd} (i.e., $L_d = L_p + L_s$). These inductances are calculated from [26]

$$L_{p,s} = \frac{\mu_0 l}{2\pi}\left[\ln\left(\frac{l}{w+t_c}\right) + 1.193 + 0.2235\left(\frac{w+t_c}{l}\right)\right] \times\left[0.57 - 0.145\ln\frac{w}{h}\right] \quad (4)$$

with w, l, and t_c referring to the width, length and conductor thickness, respectively, and h is the substrate thickness. In order to calculate L_p, the following values are used: $w = W_p$, $l = l_p/2$, $t = 0.508$ mm, and $t_c = 18$ μm. For the calculation of L_s, $w = 0.3$ mm and $l = l_{\text{sd}}$ are used. The gap capacitance C_g was calculated using the algorithm described in [24], [25]. The capacitance C_u was calculated using (3) with $A_{\text{eff}} = 1 \times 3.3$ mm^2. An initial value of L_u is obtained using (1) with Z and ϵ_{eff} being calculated using the conventional microstrip line formulas in [26] ($W = 1$ mm, $t = 0.508$ mm, and $\epsilon_r = 2.2$). The calculated values for the equivalent circuit model are listed in Table II. In order to get the excellent agreement between the circuit model and full-wave simulations observed in Fig. 7(a), the value of L_u has to be considerably tuned. The reason is that the defected pattern in the ground is expected to strongly affect the returning currents, and thus it is rather difficult to match the full-wave simulations

TABLE II

VALUES OF CIRCUIT ELEMENTS FOR THE DGS IN FIG. 7(A) (L IN nH AND C IN pF)

	L_u	L_p	L_s	C_u	C_g
Closed form	0.59 (1.1)	0.47	9.07	0.126	0.09
Tuned	4.7	0.47	9.07	0.126	0.039

TABLE III

VALUES OF CIRCUIT ELEMENTS FOR THE DGS IN FIG. 7(B) (L IN nH AND C IN pF)

	L_u	L_p	L_s	C_u	C_g
Closed form	0.3	1.4	3.96	0.252	0.045
Tuned	1	1.4	3.96	0.3	0.045

with the underestimated value of L_u obtained from the simple closed-form expression in (1). To verify this fact, and as an enhancement of our calculation of L_u, we assumed that the top lines are placed over a longitudinally slotted ground with a slot of the same width as the patch (W_p). The algorithm in [24], [25] was then used to calculate L_u. The corrected value of L_u in this case is 1.1 nH (in brackets in Table II), which is higher than the previous calculation. However, for the reasons previously mentioned, the value of L_u still needs to be tuned to achieve a good agreement between the circuit model and the full-wave simulations.

After the study of the symmetric structure above, we now analyze differential lines loaded with asymmetric DGSs; namely, the here-called *conventional* structure in Fig. 6(d) and the *glide-symmetric* structure in Fig. 6(f). As mentioned in Section II, the unit-cell of the glide-symmetric structure is obtained by translating $p_x/2$ half the unit cell in Fig. 6(d) and mirroring it with respect to the plane $y = 0$. The dimensions of the unit cells under study are the same as the ones in Fig. 6(a) with the exception of l_s, which is different from l_{sd} in order to keep the same resonance frequency. Therefore, l_s is set to 5 mm.

For the asymmetric sub-unit cell shown in the inset of Fig. 7(b), the obtaining of its equivalent circuit for the CM operation follows the same rationale as the one used for the mushroom-loaded structure in Section II-B (i.e., without even-mode symmetry). Here, L_u is calculated using (1) with $Z_{\text{CM}} = 33.9$ Ω and $\epsilon_{\text{eff}}^{\text{CM}} = 1.825$ (obtained from [23]). The capacitance C_u consists of two identical parallel capacitances, whose values are calculated from (3) with $A_{\text{eff}} = 1 \times 3.3$ mm^2. The other parameters (L_d and C_g) are calculated in a similar way to the symmetric DGS case by substituting the dimensions of the asymmetric DGS in (1) [24], [25]. The differences in the calculations here can be summarized as: 1) l_s is used instead of l_{sd} and 2) the whole length of the patch (l_p) is taken in the calculations instead of $l_p/2$. The calculated parameters for the asymmetric DGS sub-unit are summarized in Table III.

Starting from the equivalent circuit of the sub-unit cells shown in the insets of Fig. 7(a) and (b), we can now infer the one corresponding to the unit cells in Fig. 6(b), (d) and (f) by introducing a mutual capacitance and an inductive coupling (k) between the inductances L_d, as shown in Fig. 8. A very

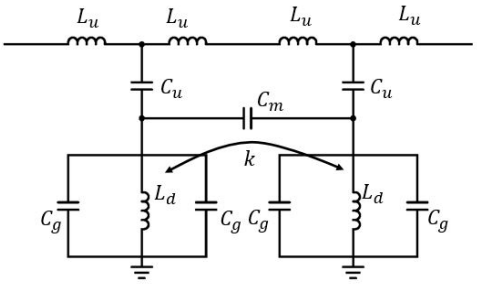

Fig. 8. Equivalent circuit for the CM operation of the DGS unit cells.

good agreement between the full-wave and equivalent-circuit results obtained for the CM operation for these unit cells can be observed in the plots shown in Fig. 9. It is worth noting that the narrow strip (connected to ground at both ends) between the ground-plane patches allows for a reduction of the electric coupling between patches as well as a better control of the magnetic coupling k between the inductances L_d [33]. In the symmetric DGS structure analyzed in [17], the electric coupling was found to be dominant as the middle strip between ground plane patches was not present. As done for the mushroom structure in the previous section, the magnetic coupling k has been extracted from full-wave simulations by means of the procedure described in [16] and [26]. For the symmetric DGS unit cell in Fig. 6(b), the coupling was found to have a mixed electric/magnetic nature resulting in $C_m = 0.0145$ pF and $k = 0.025$. For the conventional and the glide-symmetric unit cells, the electric coupling was found negligible (i.e., $C_m = 0$) with a magnetic coupling coefficient of $k_{\text{conv}} = 0.038$ and $k_{\text{glide}} = -0.055$. A stronger magnetic coupling is found in the glide-symmetric unit cell case with a change in sign due to the change in the current orientation. Altogether, a wider CM rejection bandwidth is expected for the glide-symmetric structure. It should be pointed out that all the equivalent circuit models presented in this subsection achieve a very good agreement with the full-wave simulation in terms of $|S_{11}^{\text{cc}}|$ and $|S_{21}^{\text{cc}}|$ as can be observed from Figs. 7 and 9. A similar good agreement is also found for the phase responses of $|S_{11}^{\text{cc}}|$ and $|S_{21}^{\text{cc}}|$, although not explicitly shown.

B. Unit-Cells Study and Dispersion Diagrams

In order to study the bandgap operation of the proposed asymmetric DGS structures, here we study their dispersion diagrams. For that purpose, each of the above described unit cells is simulated using *Keysight ADS Momentum* to obtain its four-port S-parameters. The mixed-mode S-parameters are then obtained from single-ended S-parameters using the transformation described in [2, Ch. 1]. Subsequently, the procedure described in [34] and [35] is exploited to obtain the dispersion diagrams for the CM operation from the CM S-parameters. The obtained dispersion diagrams of the CM for both the conventional and the glide-symmetric structures are plotted in Fig. 10. Similar to the observations in [16] and [36] and those in Section II, one can notice that the width of

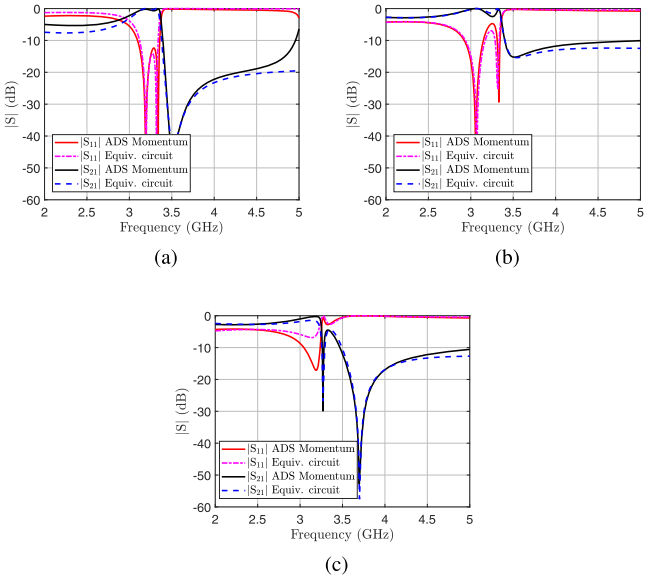

Fig. 9. Comparison of equivalent circuit vs. full-wave simulations for the CM operation of the unit cells of (a) symmetric DGS in Fig. 6(b), (b) conventional DGS in Fig. 6(d), and (c) glide-symmetric DGS in Fig. 6(f).

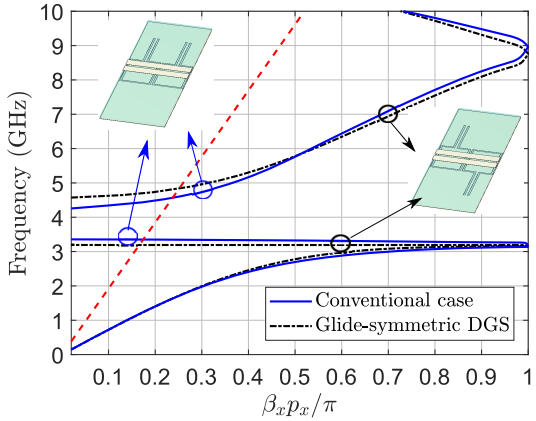

Fig. 10. Dispersion diagram for the CM operation extracted from monomodal S-parameters.

the stopband is significantly higher for the glide structure indicating a wider bandgap for the CM operation.

C. Experimental Results

In order to validate the observations from the dispersion diagram and the equivalent circuit model, finite structures of each of the three designs consisting of five unit cells in the x-direction (i.e., ten defected patterns) were simulated, fabricated, and measured. Pictures of the fabricated prototypes are provided in Fig. 11. The S-parameters for the CM and DM operation of each of the three structures have been obtained and plotted in Fig. 12 (both, simulations and measurements). It can be observed that the measured results for the three structures are in very good agreement with the simulated ones. Fig. 12(a) shows the results for the symmetric structure in Fig. 6(a). An all-pass response can be observed for the DM operation with a very good matching level

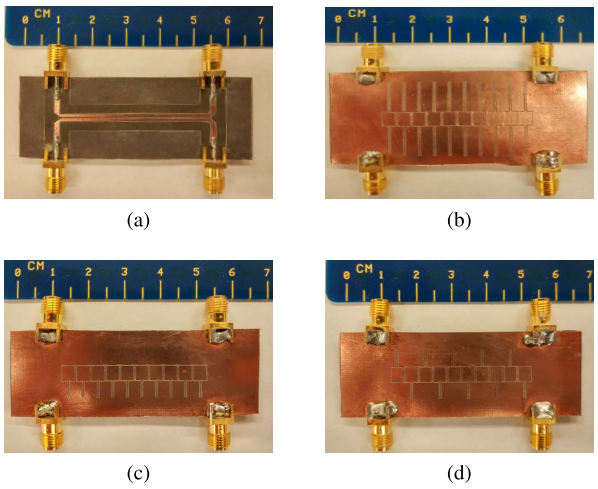

Fig. 11. Photographs of (a) top differential lines, (b) fabricated fully-symmetric DGS, (c) fabricated conventional DGS, and (d) fabricated glide-symmetric DGS.

($S_{11}^{\mathrm{dd}} < -15$ dB). The CM rejection band is found between 3.22 and 4.26 GHz, i.e. with 1.04-GHz rejection bandwidth (calculated for $S_{21}^{\mathrm{cc}} < -20$ dB). Simulated and measured results for the conventional structure [see Fig. 6(c)] are plotted in Fig. 12(b). Similar observations to the previous symmetric structure can be noticed for the DM operation. However, for the CM operation, the 20 dB rejection band is between 3.34 and 4.43 GHz, indicating a 1.09-GHz rejection bandwidth. Finally, simulated and measured results for the glide-symmetric structure [see Fig. 6(e)] are presented in Fig. 12(c), again showing a good all-pass response for the DM operation. Nevertheless, for the CM operation, a 20-dB rejection band is 3.35–4.86 GHz, i.e. a CM rejection bandwidth of 1.51 GHz, which is significantly wider than the obtained with the other two implementations.

A comparison of the measured $|S_{21}|$ for the CM operation of the three structures is shown in Fig. 13, thus making it apparent the significantly wider CM-rejection bandwidth that the glide-symmetric DGS provides.

The measured differential eye diagrams for the DM of the proposed glide-symmetric DGS structure and that of the fully symmetric DGS are shown in Fig. 14. An excitation of amplitude 0.2 V in 2.5 Gb/s was used. For the fully-symmetric DGS, the eye height, width, and opening factor are 369.35 mV, 394 ps, and 0.95, respectively. For the glide-symmetric DGS, the eye height, width, and opening factor are 367.85 mV, 392 ps, and 0.95, respectively. According to these measurements, the signal integrity of the DM in the glide-symmetric structure is almost unaltered compared to the structure possessing full longitudinal symmetry despite providing wider and stronger CM rejection.

For the sake of completeness, the proposed structures in this article are compared together and with previous literature in Table IV. In this comparison, λ_g refers to the guided wavelength at the center frequency f_o, IL_d is the insertion loss of the DM, FBW is the fractional bandwidth calculated

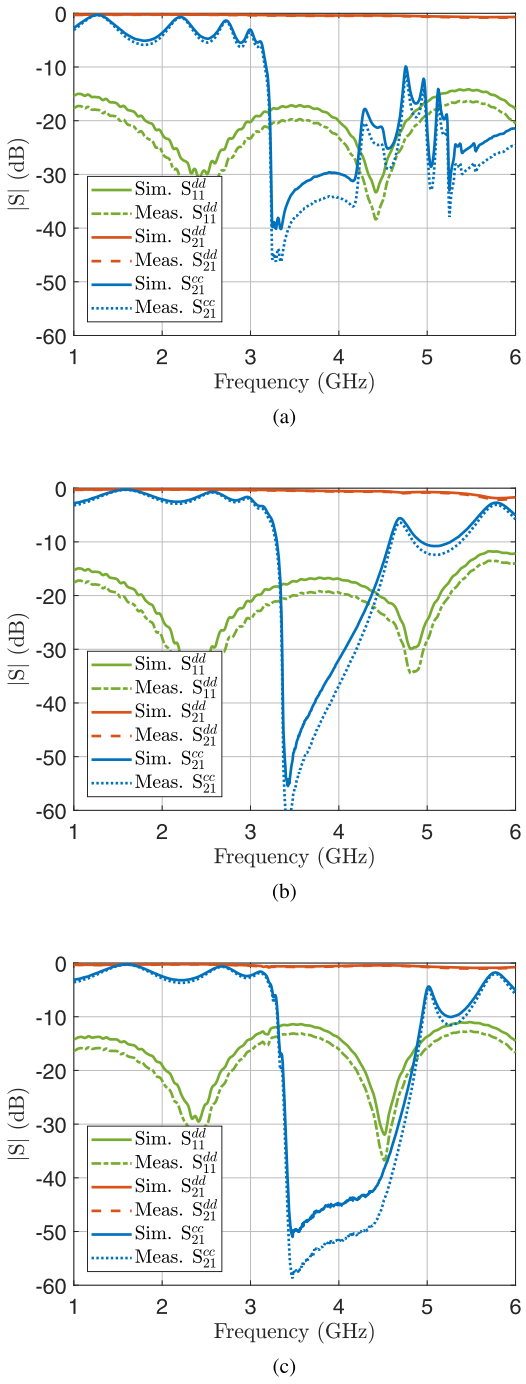

Fig. 12. Simulated and measured DM and CM responses for (a) symmetric DGS, (b) conventional DGS, and (c) glide-symmetric DGS.

at 20-dB rejection level, and CMRR_{f_o} is the CM rejection level at the center frequency. It should be pointed out that the size included in this comparison refers to the actual size of the structures excluding the feed lines. Due to the imperfections in the manufacturing process of the mushroom structures, the simulated CMRR is included in brackets as well. Although the main purpose of this work was to investigate the effect of applying glide symmetry to CM rejection filters and not to design a perfect filter, it can be noticed that the proposed glide-symmetric structures offer competitive performance in

TABLE IV
COMPARISON WITH PREVIOUSLY REPORTED DIFFERENTIAL LINES WITH CM REJECTION

Ref	Process	Size ($\lambda_g \times \lambda_g$)	f_o (GHz)	IL_d (dB)	FBW (-20dB) %	$CMRR_{f_o}$(dB)
[37]	2-layer PCB	0.64×0.13	1.37	-	41	50
[38]	2-layer PCB	0.58×0.14	4.8	< 0.5 (0.2 @f_o)	61	40
[39]	LTCC	0.26×0.16	5.45	< 1	32	35
[12]	2-layer PCB	0.09×0.37	1.3	< 1.5	57.7	55
Conv. Mush.	3-layer PCB	1.4×0.373	3	< 0.9 (0.66 @f_o)	21.6	27 (simu. 41)
Glide Mush.	3-layer PCB	1.4×0.373	3	< 0.9 (0.62 @f_o)	32.5	36 (simu. 48)
Full symm. DGS	2-layer PCB	0.65×0.42	3.3	< 0.8 (0.37 @f_o)	31.5	44
Conv. DGS	2-layer PCB	0.65×0.39	3.3	< 0.8 (0.35 @f_o)	33	52
Glide. DGS	2-layer PCB	0.65×0.39	3.3	< 0.8 (0.6 @f_o)	45.7	50

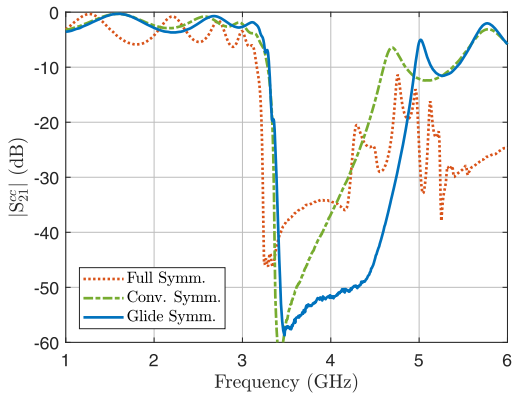

Fig. 13. Comparison of the measured CM response for the three structures under study.

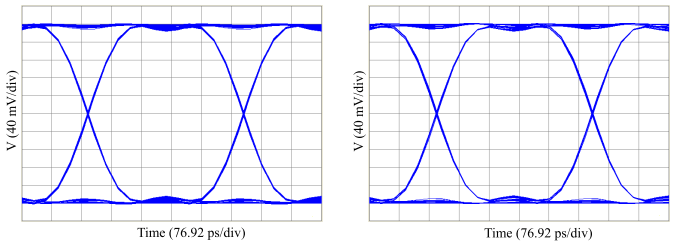

Fig. 14. Measured eye diagrams for the DM of (a) fully-symmetric DGS and (b) glide-symmetric DGS.

terms of FBW, $CMRR_{f_o}$ as well as a very low insertion loss for the DM. Moreover, it is worth mentioning that the relatively large size of the proposed structures was mainly to mimic the performance of a periodic structure and can be further reduced by reducing the number of unit cells or using a substrate of a higher dielectric constant. As a final note, we would like to mention that the proposed defected ground structures are easier and cheaper to fabricate since laminating multilayer stack or hidden-via holes are not required. This means that if cost is a major requirement, DGSs are more convenient. On the contrary, if a structure with a solid ground plane to avoid external interference is required, a multilayer mushroom structure is preferred.

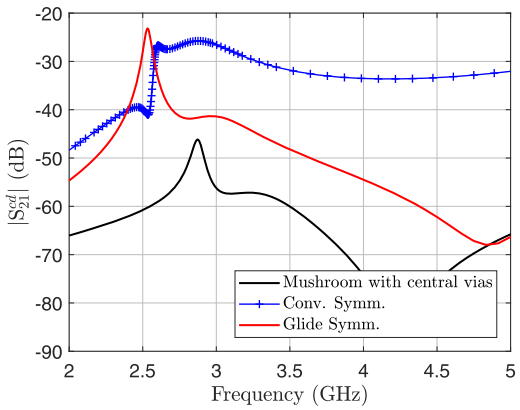

Fig. 15. Comparison of the mixed-mode response for unit cells of the mushroom structures simulated using *ADS Momentum*: fully symmetric with central vias, conventional edge-located vias and glide-symmetric edge vias.

IV. CONCLUSION

The application of glide symmetry to CM rejection filters has been studied in this work. Specifically, differential lines loaded with a glide-symmetric mushroom structure as well as differential lines loaded with a glide-symmetric DGS have been proposed. A full study of each of the considered structures is carried out in terms of dispersion diagrams, equivalent circuit model, full-wave simulation, and measurements. The proposed structures have demonstrated that glide symmetry can conveniently improve CM rejection bandwidth without affecting the performance of the DM or adding any extra manufacturing costs. This fact has been verified through measurements of manufactured prototypes of each studied structure. Investigating the application of glide symmetry in other configurations of differential filters is open for future research.

APPENDIX

As discussed previously in the article, the proposed structures do not possess a longitudinal symmetry plane in contrast with conventional CM rejection filters. Therefore, it is important to study the mode conversion between the DM and CM to ensure their suitability to work as CM rejection filters. For that purpose, we have evaluated the mixed-mode *S*-parameters for one unit cell of each of the structures under study. In Fig. 15, the mixed-mode *S*-parameter is plotted

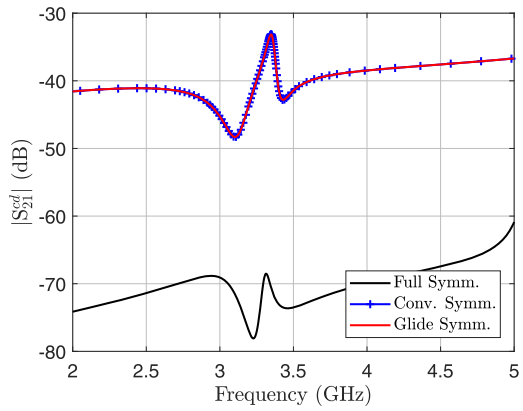

Fig. 16. Comparison of the mixed-mode response for unit cells of the DGS structures: fully-symmetric, conventional symmetry and glide-symmetric.

for differential lines loaded with: 1) fully-symmetric mushrooms with central vias; 2) mushrooms with conventional edge-located vias; and 3) mushrooms with glide-symmetric edge-located vias. Although $|S_{21}^{cd}|$ is higher for the cases of conventional and glide-symmetric edge-located vias than for the case of full symmetry, it is sufficiently low to neglect the mixed-mode excitation, which confirms the suitability of the proposed mushroom structures to work as CM rejection filters. A similar conclusion can be drawn from Fig. 16 for the DGS structure, also confirming the low level of mode conversion in the proposed DGS structure with glide symmetry.

ACKNOWLEDGMENT

The authors would like to thank the EEE Parts Laboratory Department of Alter Technology Tüv Nord and, in particular, Dr. A. Lujambio for the help during the eye diagram measurements. This article is also based upon work from COST Action SyMat CA18223, supported by COST (European Cooperation in Science and Technology), www.cost.eu.

REFERENCES

[1] F. Martín *et al.*, "The beauty of symmetry: Common-mode rejection filters for high-speed interconnects and band microwave circuits," *IEEE Microw. Mag.*, vol. 18, no. 1, pp. 42–55, Jan. 2017.

[2] F. Martín, L. Zhu, J. Hong, and F. Medina, *Balanced Microwave Filters*. Hoboken, NJ, USA: Wiley, 2018.

[3] W. Feng, W. Che, and Q. Xue, "New balance-applications for dual-mode ring resonators in planar balanced circuits," *IEEE Microw. Mag.*, vol. 20, no. 7, pp. 15–23, Jul. 2019.

[4] F. Lin, W. Feng, and X. Tan, "Tunable balanced power dividers," *IEEE Microw. Mag.*, vol. 22, no. 2, pp. 46–56, Feb. 2021.

[5] H. Zhu, P. Qin, and Y. J. Guo, "Single-ended-to-balanced power divider with extended common-mode suppression and its application to differential 2 × 4 Butler matrices," *IEEE Trans. Microw. Theory Techn.*, vol. 68, no. 4, pp. 1510–1519, Apr. 2020.

[6] W. Feng *et al.*, "Balanced rat-race couplers with wideband common-mode suppression," *IEEE Trans. Microw. Theory Techn.*, vol. 67, no. 12, pp. 4724–4732, Dec. 2019.

[7] J. Martel, A. Fernandez-Prieto, J. L. M. del Rio, F. Martin, and F. Medina, "Design of a differential coupled-line directional coupler using a double-side coplanar waveguide structure with common-signal suppression," *IEEE Trans. Microw. Theory Techn.*, vol. 69, no. 2, pp. 1273–1281, Feb. 2021.

[8] L.-L. Qiu, L. Zhu, and Y.-P. Lyu, "Balanced wideband phase shifters with wide phase shift range and good common-mode suppression," *IEEE Trans. Microw. Theory Techn.*, vol. 67, no. 8, pp. 3403–3413, Aug. 2019.

[9] X. Guan, B. Zhao, and B. Ren, "Dual-band differential bandpass filters using quadruple-mode stubs-loaded ring resonator with intrinsic common-mode suppression for 5G," *IEEE Access*, vol. 8, pp. 205550–205557, 2020.

[10] C. Chan and T. Wu, "A high-performance common-mode noise absorption circuit based on phase modification technique," *IEEE Trans. Microw. Theory Techn.*, vol. 67, no. 11, pp. 4394–4403, Nov. 2019.

[11] P.-J. Li and T.-L. Wu, "A novel circuit architecture of bidirectional common-mode noise absorption circuit," *IEEE Trans. Microw. Theory Techn.*, vol. 68, no. 4, pp. 1476–1486, Apr. 2020.

[12] A. Ebrahimi, T. C. Baum, K. Wang, J. Scott, and K. Ghorbani, "Differential transmission lines loaded with magnetic LC resonators and application in common mode suppression," *IEEE Trans. Circuits Syst.*, vol. 66, no. 10, pp. 3811–3821, Oct. 2019.

[13] A. Ebrahimi, W. Withayachumnankul, S. F. Al-Sarawi, and D. Abbott, "Dual-mode behavior of the complementary electric-LC resonators loaded on transmission line: Analysis and applications," *J. Appl. Phys.*, vol. 116, no. 8, 2014, Art. no. 083705.

[14] I. Shahid, D. Thalakotuna, and M. Heimlich, "A bi-patch loaded microstrip line based 1-D periodic structure with enhanced stop bandwidth and band switching characteristics," *J. Electromagn. Waves Appl.*, vol. 33, no. 10, pp. 1329–1342, Jul. 2019.

[15] I. Shahid, D. N. Thalakotuna, D. K. Karmokar, and M. Heimlich, "Asymmetric transversal patch loaded microstrip line based 1-D periodic structure with flexible selection of stopband resonance," *AEU-Int. J. Electron. Commun.*, vol. 114, Feb. 2020, Art. no. 153010.

[16] B. A. Mouris, A. Fernández-Prieto, R. Thobaben, J. Martel, F. Mesa, and O. Quevedo-Teruel, "On the increment of the bandwidth of mushroom-type EBG structures with glide symmetry," *IEEE Trans. Microw. Theory Techn.*, vol. 68, no. 4, pp. 1365–1375, Apr. 2020.

[17] A. Fernandez-Prieto *et al.*, "Dual-band differential filter using broadband common-mode rejection artificial transmission line," *Prog. Electromagn. Res.*, vol. 139, pp. 779–797, 2013.

[18] D. Sievenpiper, L. Zhang, R. F. J. Broas, N. G. Alexopolous, and E. Yablonovitch, "High-impedance electromagnetic surfaces with a forbidden frequency band," *IEEE Trans. Microw. Theory Techn.*, vol. 47, no. 11, pp. 2059–2074, Nov. 1999.

[19] L. Yang, M. Fan, F. Chen, J. She, and Z. Feng, "A novel compact electromagnetic-bandgap (EBG) structure and its applications for microwave circuits," *IEEE Trans. Microw. Theory Techn.*, vol. 53, no. 1, pp. 183–189, Jan. 2005.

[20] N. Yang, Z. N. Chen, Y. Wang, and M. Y. W. Chia, "A two-layer compact electromagnetic bandgap (EBG) structure and its applications in microstrip filter design," *Microw. Opt. Technol. Lett.*, vol. 37, no. 1, pp. 62–64, Apr. 2003.

[21] E. Rajo-Iglesias, L. Inclan-Sanchez, J.-L. Vazquez-Roy, and E. Garcia-Munoz, "Size reduction of mushroom-type EBG surfaces by using edge-located vias," *IEEE Microw. Wireless Compon. Lett.*, vol. 17, no. 9, pp. 670–672, Sep. 2007.

[22] M. C. Velazquez-Ahumada, J. Martel, and F. Medina, "Design of compact low-pass elliptic filters using double-sided MIC technology," *IEEE Trans. Microw. Theory Techn.*, vol. 55, no. 1, pp. 121–127, Jan. 2007.

[23] EEWeb. *Calculator for Edge Coupled Microstrip Impedance*. Accessed: Feb. 23, 2021. [Online]. Available: https://eeweb.com/tools/edge-coupled-microstrip-impedance/

[24] J. Martel and F. Medina, "A suitable integral equation for the quasi-TEM analysis of hybrid strip/slot-like structures," *IEEE Trans. Microw. Theory Techn.*, vol. 49, no. 1, pp. 224–227, Jan. 2001.

[25] J. Martel, R. R. Boix, and M. Horno, "Static analysis of microstrip discontinuities using the excess charge density in the spectral domain," *IEEE Trans. Microw. Theory Techn.*, vol. 39, no. 9, pp. 1623–1631, Sep. 1991.

[26] J. Hong and M. Lancaster, *Microstrip Filters for RF/Microwave Applications* (Wiley Series in Microwave and Optical Engineering). Hoboken, NJ, USA: Wiley, 2001.

[27] M. E. Goldfarb and R. A. Pucel, "Modeling via hole grounds in microstrip," *IEEE Microw. Guided Wave Lett.*, vol. 1, no. 6, pp. 135–137, Jun. 1991.

[28] J.-S. Hong and M. J. Lancaster, "Couplings of microstrip square open-loop resonators for cross-coupled planar microwave filters," *IEEE Trans. Microw. Theory Techn.*, vol. 44, no. 11, pp. 2099–2109, Nov. 1996.

[29] J. Martínez, A. Coves, F. Mesa, and O. Quevedo-Teruel, "Pass-band broadening of sub-wavelength resonator-based glide-symmetric SIW filters," *AEU-Int. J. Electron. Commun.*, vol. 125, Oct. 2020, Art. no. 153362.

[30] V. Radisic, Y. Qian, R. Coccioli, and T. Itoh, "Novel 2-D photonic bandgap structure for microstrip lines," *IEEE Microw. Guided Wave Lett.*, vol. 8, no. 2, pp. 69–71, Feb. 1998.

[31] D. Ahn, J. S. Park, C. S. Kim, J. Kim, Y. Qian, and T. Itoh, "A design of the low-pass filter using the novel microstrip defected ground structure," *IEEE Trans. Microw. Theory Techn.*, vol. 49, no. 1, pp. 86–93, Jan. 2001.

[32] A. C. Durgun, C. A. Balanis, C. R. Birtcher, H. Huang, and H. Yu, "High-impedance surfaces with periodically perforated ground planes," *IEEE Trans. Antennas Propag.*, vol. 62, no. 9, pp. 4510–4517, Sep. 2014.

[33] A. Fernández-Prieto, J. Bhatker, A. Lujambio, J. Martel, F. Medina, and R. R. Boix, "Balanced bandpass filter based on magnetically coupled coplanar waveguide folded-stepped impedance resonators," *Electron. Lett.*, vol. 52, no. 14, pp. 1229–1231, Jul. 2016.

[34] G. Valerio, S. Paulotto, P. Baccarelli, P. Burghignoli, and A. Galli, "Accurate Bloch analysis of 1-D periodic lines through the simulation of truncated structures," *IEEE Trans. Antennas Propag.*, vol. 59, no. 6, pp. 2188–2195, Jun. 2011.

[35] F. Mesa, G. Valerio, R. Rodriguez-Berral, and O. Quevedo-Teruel, "Simulation-assisted efficient computation of the dispersion diagram of periodic structures: A comprehensive overview with applications to filters, leaky-wave antennas and metasurfaces," *IEEE Antennas Propag. Mag.*, vol. 63, no. 5, pp. 33–45, Oct. 2021, doi: 10.1109/MAP.2020.3003210.

[36] B. A. Mouris, A. Fernández-Prieto, R. Thobaben, J. Martel, F. Mesa, and O. Quevedo-Teruel, "Glide symmetry to improve the bandgap operation of periodic microstrip defected ground structures," in *Proc. 50th Eur. Microw. Conf. (EuMC)*, 2021, pp. 483–486.

[37] J. Naqui *et al.*, "Common-mode suppression in microstrip differential lines by means of complementary split ring resonators: Theory and applications," *IEEE Trans. Microw. Theory Techn.*, vol. 60, no. 10, pp. 3023–3034, Oct. 2012.

[38] J. Martel, A. Fernández-Prieto, A. Lujambio, F. Medina, F. Mesa, and R. R. Boix, "Differential lines for common-mode suppression based in hybrid microstrip/CPW technology," *IEEE Microw. Wireless Compon. Lett.*, vol. 27, no. 1, pp. 13–15, Jan. 2017.

[39] C.-H. Tsai and T.-L. Wu, "A broadband and miniaturized common-mode filter for gigahertz differential signals based on negative-permittivity metamaterials," *IEEE Trans. Microw. Theory Techn.*, vol. 58, no. 1, pp. 195–202, Jan. 2010.

Boules A. Mouris (Member, IEEE) was born in Cairo, Egypt. He received the B.Sc. and M.Sc. degrees in electronics and communications engineering from Cairo University, Giza, Egypt, in 2013 and 2016, respectively. He is currently pursuing Ph.D. degree at the Division of Information Science and Engineering, School of Electrical Engineering and Computer Science, KTH Royal Institute of Technology, Stockholm, Sweden.

His current research interests include high-symmetric periodic structures, metasurfaces, intelligent reflecting surfaces, antenna design, simultaneous wireless information and power transfer, and wireless powered communication systems.

Armando Fernández-Prieto (Senior Member, IEEE) was born in Ceuta, Spain, in September 1981. He received the Licenciado and Ph.D. degrees in physics from the Universidad de Sevilla, Seville, Spain, in 2007 and 2013, respectively.

He is currently an Assistant Professor of electromagnetism with the Department of Electronics and Electromagnetism, University of Seville, and a member of the Microwaves Group. His research interests focus on printed passive microwave components and metamaterials.

Dr. Fernández-Prieto is a Reviewer for the IEEE TRANSACTIONS ON MICROWAVE THEORY AND TECHNIQUES, the IEEE MICROWAVES AND WIRELESS COMPONENTS LETTERS, the IEEE TRANSACTIONS ON ANTENNAS AND PROPAGATIONS, and IEEE ACCESS, as well as for many other journals.

Jose L. Medrán del Río (Graduate Student Member, IEEE) was born in Puertollano, Ciudad Real, Spain, in 1994. He received the bachelor's degree in telecommunication technologies and services engineering, the master's degree in telecommunication technologies, systems and networks, and the master's degree in telecommunication engineering from the Universitat Politècnica de València in 2016, 2018, and 2019, respectively. He is currently pursuing the Ph.D. degree at the Electronics and Electromagnetism Department, Universidad de Sevilla, Seville, Spain.

His research focuses on new configurations of planar differential microwave devices for multiband applications.

Ragnar Thobaben (Member, IEEE) received the Dr.-Ing. (Ph.D.) degree in electrical engineering from the Christian-Albrechts-University of Kiel, Kiel, Germany, in 2007.

In 2006, he joined the KTH Royal Institute of Technology, Stockholm, Sweden, as a Post-Doctoral Researcher, where he is currently an Associate Professor. He has researched various topics such as cognitive radio, cooperative communication, coordination, and security. His current research focuses on physical-layer security, simultaneous wireless energy and information transfer, as well as signal processing, information theory, and coding theory applied to problems in communications and learning.

Dr. Thobaben has served on the Technical Program Committee for several IEEE conferences, such as GLOBECOM, ICC, and PIMRC. He has served on the Technical Program Committee for several IEEE conferences, such as GLOBECOM, ICC, and PIMRC. He has also served as the Publicity Chair for the 2011 IEEE Swedish Communication Technologies Workshop, the 2012 International Symposium on Turbo Codes and Iterative Information Processing, and the 2015 IEEE International Workshop on Signal Processing Advances in Wireless Communications (SPAWC), and as the local-arrangement chair for the 2019 IEEE Information Theory Workshop (ITW). From 2016 to 2020, he served as an Editor for the IEEE TRANSACTIONS ON COMMUNICATIONS, and since 2020, he has been serving as an Editor for the IEEE TRANSACTIONS ON INFORMATION FORENSICS AND SECURITY.

Jesús Martel (Senior Member, IEEE) received the Licenciado and Ph.D. degrees in physics from the University of Sevilla, Seville, Spain, in 1989 and 1996, respectively.

Since 1990, he has performed research with the Microwave Group, University of Sevilla. He is currently a Professor with the Department of Applied Physics II, University of Sevilla, where he was the Head of the Department from 2010 to 2018. His current research interests are focused on the numerical analysis of planar transmission lines, the modeling of planar microstrip discontinuities, the design of passive microwave circuits, the techniques in microwave measurements, and the proprieties of artificial media.

Francisco Mesa (Fellow, IEEE) received the Licenciado and Ph.D. degrees in physics from the Universidad de Sevilla, Seville, Spain, in 1989 and 1991, respectively.

He is currently a Professor with the Departamento de Física Aplicada 1, Universidad de Sevilla. His current research interests include electromagnetic propagation/radiation in planar structures.

Francisco Medina (Fellow, IEEE) was born in Puerto Real, Cadiz, Spain, in November 1960. He received the M.Sc. and Ph.D. degrees in physics (electronics) from the University of Sevilla, Seville, Spain, in 1983 and 1987, respectively.

He has been a Visiting Scholar with ENSEEIHT, INP, Toulouse, France, and Queen Mary University of London, London, U.K. He is currently a Professor of electromagnetism with the Department of Electronics and Electromagnetism, Physics Faculty, University of Sevilla, where he teaches topics related to electromagnetism. He is also the Head of the Microwaves Group. His research has been focused on analytical and numerical methods for the modeling of planar structures, passive planar circuits, and modeling of periodic structures and metamaterials.

Dr. Medina is currently the Editor in Chief of *International Journal of Microwave and Wireless Technologies*, and acts as a Reviewer for many journals in the fields of microwave and antenna engineering, optics, and applied physics. He co-organized the 2017 IEEE-MTT NEMO Symposium (Seville, Spain) and collaborates as a TPC Member or Reviewer with a number of national and international conferences, including the URSI Spanish Symposium and the European Microwave Week. Since 2017, he has been the President of the Spanish URSI Committee.

Oscar Quevedo-Teruel (Senior Member, IEEE) received the degree in Telecommunications Engineering and the Ph.D. degree from the Carlos III University of Madrid, Madrid, Spain, in 2005 and 2010, respectively.

From 2010 to 2011, he joined the Department of Theoretical Physics of Condensed Matter, Universidad Autonoma de Madrid as a Research Fellow and went on to continue his post-doctoral research with the Queen Mary University of London, London, U.K., from 2011 to 2013. In 2014, he joined the Division for Electromagnetic Engineering, School of Electrical Engineering and Computer Science, KTH Royal Institute of Technology, Stockholm, Sweden, where he is a Professor and the Director of the Master Program in electromagnetics fusion and space engineering. He has made scientific contributions to higher symmetries, transformation optics, lens antennas, metasurfaces, leaky wave antennas and high impedance surfaces. He is the coauthor of more than 100 articles in international journals and 150 at international conferences.

Dr. Quevedo-Teruel has been an Associate Editor of the IEEE TRANSACTIONS ON ANTENNAS AND PROPAGATION since 2018 and has been the Founder and Editor-in-Chief of the *EurAAP Journal Reviews of Electromagnetics* since 2020. He was the EurAAP delegate for Sweden, Norway, and Iceland from 2018 to 2020 and he has been a member of the EurAAP Board of Directors since January 2021. He is a Distinguished Lecturer of the IEEE Antennas and Propagation Society from 2019 to 2021 and a Chair of the IEEE APS Educational Initiatives Program since 2020.